THE JOURNAL OF BIOLOGICAL CHEMISTRY VOL. 284, NO. 11, pp. 7177–7189, March 13, 2009

Curvature Dynamics of α-Synuclein Familial Parkinson Disease Mutants

MOLECULAR SIMULATIONS OF THE MICELLE- AND BILAYER-BOUND FORMS[*S]

Received for publication, November 24, 2008, and in revised form, December 30, 2008 Published, JBC Papers in Press, January 5, 2009, DOI 10.1074/jbc.M808895200

Jason D. Perlmutter, Anthony R. Braun, and Jonathan N. Sachs[1]

From the Department of Biomedical Engineering, University of Minnesota, Minneapolis, Minnesota 55455

α-Synuclein remains a protein of interest due to its propensity to form fibrillar aggregates in neurodegenerative disease and its putative function in synaptic vesicle regulation. Herein, we present a series of atomistic molecular dynamics simulations of wild-type α-synuclein and three Parkinson disease familial mutants (A30P, A53T, and E46K) in two distinct environments. First, in order to match recent NMR experiments, we have simulated each protein bound to an SDS detergent micelle. Second, in order to connect more closely to the true biological environment, we have simulated the proteins bound to a 1,2-dioleoyl-*sn*-glycero-3-phosphoserine lipid bilayer. In the micelle-bound case, we find that the wild type and all of the variants of α-synuclein flatten the underlying micelle, decreasing its surface area. A30P is known to lessen α-synuclein/membrane affinity and, consistent with experiment, destabilizes the simulated secondary structure. In the case of A53T, our simulations reveal a range of stabilizing hydrogen bonds that form with the threonine. In both environments, the E46K mutation, which is known to increase bilayer affinity, leads to an additional hydrogen bond between the protein and either the detergent or lipid. Simulations indicate that αS and its variants are less dynamic in the bilayer than in the micelle. Furthermore, the simulations of the mutants suggest how changes in the structure and dynamics of α-synuclein may affect its biological role.

The main component of fibrous inclusions known as Lewy bodies and Lewy neurites, α-synuclein (αS)[2] plays a critical, although as yet not fully understood, role in the onset of Parkinson disease (PD) (1). Three point mutations of αS, namely A53T, A30P, and E46K, have been correlated with familial PD (2–4), although it is still unclear exactly how these mutations trigger the disease (5–8). In the case of A30P, a set of recent NMR studies suggest that the proline substitution significantly increases the structural dynamics of the protein when bound to an SDS detergent micelle (9, 10). It is widely accepted that this mutant has reduced binding affinity for membranes, although the extent is somewhat controversial (9, 11–17). The change in membrane affinity is correlated with a decrease in the helical content of the protein, although again there is considerable debate as to the extent of this effect (9, 10, 13, 16, 18). This result is not altogether unexpected; proline disrupts helices due to the loss of a backbone hydrogen bond and steric hindrance between it and neighboring residues (19). The exact effects of proline on a helix, however, can be 2-fold: substitution can cause local unfolding (*i.e.* total loss of secondary structure) or kinking without loss of helicity. In the case of A30P, current experimental techniques have suggested a loss of helicity up- and downstream of the substitution. However, it is still unclear to what extent and where the proline substitution forces unfolding, kinking, or both (9, 10).

The other PD familial mutants behave quite differently. The threonine substitution does not disrupt αS affinity for either synthetic vesicles or cellular membranes (9, 11–13, 15–17). Likewise, the mutation does not appear to impact the protein's secondary structure (*i.e.* helicity is fully conserved) (9, 10, 13, 16, 18). The more recently discovered E46K mutation leads to tighter binding between the protein and synthetic vesicles (20) while also preserving the secondary structure (21). How these three mutations exert such divergent affects yet are each linked to PD remains an open question. Although the function of αS remains unknown, localization to synaptic vesicles (12, 22, 23) has led to investigation of its role in synaptic vesicle regulation (24–28). Therefore, changes in membrane affinity or protein structure may alter the functionality of αS and may be a significant factor in PD pathogenesis (29).

Structurally, the N-terminal domain (residues 1–99) of WT αS forms two anti-parallel amphipathic helices on the membrane surface (30, 31). The acidic C-terminal domain (residues 100–140) does not participate in membrane binding and remains unstructured (32, 33). Truncation of the protein beyond residue 99 has no affect on the structure or binding properties of the N-terminal domain (9). When bound to an SDS micelle, the two helices, connected by an unstructured loop, are unusually dynamic and highly curved (the C-terminal helix (helix-C) being nearly twice as curved as its N-terminal (helix-N) counterpart) (34). This micelle-bound structure is not nearly as curved as the unperturbed, spherical SDS micelle, and the degree of curvature is probably of functional significance. It was speculated, although not proven, that binding of αS deforms a micelle in a uniaxial direction, forcing an ellipsoidal rather than spherical structure (34). This invites a highly

* The costs of publication of this article were defrayed in part by the payment of page charges. This article must therefore be hereby marked "*advertisement*" in accordance with 18 U.S.C. Section 1734 solely to indicate this fact.

[S] The on-line version of this article (available at http://www.jbc.org) contains supplemental Figs. S1–S5.

[1] To whom correspondence should be addressed: 312 Church St. S.E., 7-126 Hasselmo Hall, Minneapolis, MN 55455. Fax: 612-626-6583; E-mail: jnsachs@umn.edu.

[2] The abbreviations used are: αS, α-synuclein; PD, Parkinson disease; WT, wild type; MD, molecular dynamics; r.m.s.d., root mean square deviation; r.m.s.f., root mean square fluctuation; DOPS, 1,2-dioleoyl-*sn*-glycero-3-phosphoserine; NAC, non-Aβ component of Alzheimer disease amyloid.

attractive hypothesis; protein-induced membrane deformation may underlie αS function, in particular as regards the potential impact such deformations may have on membrane fusion and the formation of fusion intermediates.

Computational molecular dynamics (MD) simulation is an excellent tool for characterizing the structural and dynamic features of proteins. MD simulations are capable of revealing molecular level detail inaccessible to current high resolution experimental methods and can therefore illuminate unresolved issues connecting a protein's structure to its biological function. Because the function of αS appears so tightly coupled to dynamic changes in its structure, MD is an ideal tool for studying this system. Indeed, four recent MD simulations of αS have provided tremendous insight into the behavior of the WT protein. In particular, simulations have revealed a broad distribution of natively unfolded structures in solution; mapped specific, stabilizing contact points within those structures (35); elucidated the behavior of WT αS on the surface of membranes, in one case calculating the energetics of membrane binding (36) and in another suggesting a novel homo-oligomeric organization (37); and described the behavior of the interhelical turn region in multiple environments (38).

The goal of this current study has been to use MD simulation to uncover experimentally inaccessible information regarding structural and dynamic changes to αS induced by the A53T, A30P, and E46K mutations. Collectively, our simulation results confirm and expand upon the existing perceptions regarding the PD mutants. The first set of simulations starts with the recently solved, high resolution NMR structure of WT αS bound to an SDS micelle, where great care has been taken to accurately reproduce the experimental system (34). We find that protein binding elongates the micelle, relieving curvature stress and suggesting a functional role for WT αS. Helical bending, in particular at the site of consecutive glycine residues, endows αS with the conformational flexibility necessary to bind to membranes with variable curvature. Simulations of the mutant forms are analyzed in terms of local and long range changes in dynamics and structure.

Significant questions remain about directly transferring the insight derived from micelle studies to the character of αS in biological membranes. Two recent experimental studies suggest that the structure of the membrane-bound form of αS is similar to that of the micelle form (*i.e.* contains the same broken helix structural motif) (38, 39). These experiments provide a good rationale for designing our second set of simulations, in which we have studied the dynamics of αS and the three mutants bound to a DOPS bilayer using the simulated, micelle-bound structure of WT αS as our starting configuration. We have chosen phosphatidylserine because of the high affinity of αS for anionic phospholipids (31). A comparison of our results for the highly curved micelle and the flatter bilayer patch suggests that αS probably adapts to biological membranes of intermediate curvature (*e.g.* synaptic vesicles) by modulating the degree of bending at specific flexible sites.

MATERIALS AND METHODS

Micelle-bound Simulations—The starting configuration for the αS protein was the structure as determined by high resolution NMR (Protein Data Bank code 1XQ8 (34)). For the micelle simulation, a pre-equilibrated, fully hydrated micelle consisting of 100 SDS detergent molecules was positioned a few Å away. Initial WT simulations were run using an SDS micelle composed of 70 SDS molecules, the reported average size from experiments (30, 34). However, despite considerable effort, we were unable to stabilize the protein on this micelle and thus nominally increased its size. The protein was positioned with the hydrophobic surface facing the micelle so as to match their concavities, building in an assumption regarding their relative orientations that is fully reasonable given the results of the NMR study (34). The protein includes only the N-terminal domain, residues 1–99. Fig. 1 gives the primary amino acid sequence for the simulated protein and highlights the key structural segments as well as positions of the point mutants. This system was solvated in a water box consisting of ~23,000 TIP3 water molecules, with several layers of water molecules separating the protein and micelle. The average size of the simulation cell (90 × 90 × 90 Å) was carefully determined based upon the minimum-image convention so as to avoid finite size artifacts and included 100 sodium cations and additional chloride anions to neutralize the overall charge of the system. Thus, the solvated protein/micelle simulations consisted of ~76,000 atoms. Control simulations of a solvated, detergent-free WT α-synuclein and a protein-free, solvated micelle consisted of ~69,000 atoms and ~74,000 atoms, respectively.

MDVFMKGLSKAKEGVVAAAEKTKQGVAEAAGKTK
EGVLYVGSKTKEGVVHGVATVAEKTKEQVTNVGGA
VVTGVTAVAQKTVEGAGSIAAATGFVKKDQ

FIGURE 1. **Amino acid sequence of membrane binding domain of αS.** Only the first 99 amino acids are involved in lipid binding and were considered in these simulations. *Underlined* are the two helices in the lipid binding domain. The positions in the wild-type where the PD familial mutations occur are in *boldface type*. The highly hydrophobic NAC region consisting of residues 60–95 is in *italic type*.

The micelle-bound systems were constructed and analyzed using CHARMM version 32 with the CMAP correction. Periodic boundary conditions were applied, using a constant number of atoms (*N*), pressure (*P*), and temperature (*T*), to form NPT ensembles. The temperature in each simulation was set to 303 K. Simulations were performed using NAMD version 2.6. A cut-off of 10 Å was used for van der Waals interactions, and particle mesh Ewald summation was used for long range electrostatic interactions. The time step was 2 fs, and all bonds involving hydrogen were fixed using the SHAKE algorithm. The molecules were visualized with VMD (40), and secondary structure was calculated with the Stride algorithm (41), which assigns secondary structure from a given coordinate set based upon hydrogen bonds and torsion angles.

Because the structure of αS does not provide direct information regarding the configuration of the SDS micelle, we employed a strategy of protein restraints in order to allow the proteins to bind to and equilibrate within the micelle. Specifically, the systems were first energy-minimized and then simulated for 20 ns with the protein under a restraint to prevent unfolding. During the course of these 20 ns, the micelle, which was not restrained, morphed into contact with the protein, forming two deep channels into which the two helices buried. The simulation was then run in this bound

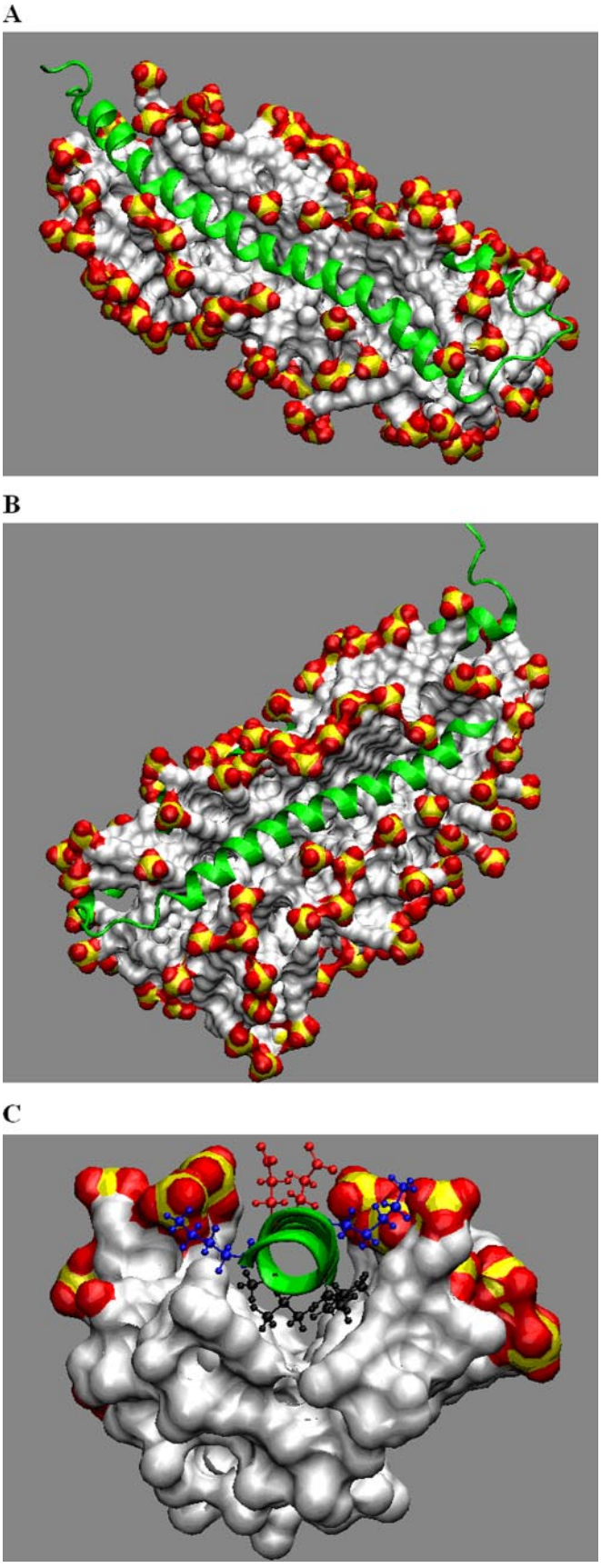

FIGURE 2. **The interaction of αS with an SDS micelle.** *A* and *B*, snapshots of wild-type αS bound to the detergent micelle, after 45 ns of simulated dynamics. The protein embeds deeply into the core of the micelle, forming channels in both helix-C (*A*) and helix-N (*B*). *C*, a representative slice through the micelle, illustrating typical side chain orientations. Nonpolar side chains are directed toward the micelle center, basic side chains orient along the micelle surface, and acidic side chains orient toward the water. αS backbone is represented as a *green ribbon*, and side chains are represented with the following *colors*: nonpolar (*black*), basic (*blue*), and acidic (*red*). The SDS micelle is shown with the following *color scheme*: carbon (*white*), sulfur (*yellow*), and oxygen (*red*). Hydrogens, water, and ions have been removed for clarity of presentation.

state without restraint for 45 ns. Thus, each αS/micelle system was run for a total of 65 ns, although only the unrestrained simulation was used for analysis. The protein-free and micelle-free systems were each run for 10 ns, where in the case of the protein-free system the micelle's radius of gyration was deemed converged (data not shown), and in the micelle-free system the r.m.s.d. of the protein clearly contrasted with the stability of the micelle-bound protein.

In order to construct the A30P, A53T, and E46K mutants, the starting configuration of the system was the same as WT (*i.e.* the NMR structure), with only the side chains of the appropriate residues substituted. The orientation of the substituted residue was determined by the coordinates of the WT side chain, and additional atoms were added using the CHARMM force field parameters for bonds, angles, and dihedrals. These two simulations were set up and run using the identical conditions and strategy of restraints and dynamics described for the WT.

Bilayer-bound Simulations—The bilayer-bound systems were constructed by placing the final structure of the WT micelle-bound protein in the headgroup region of a pre-equilibrated pure DOPS bilayer (containing 512 lipids and ~17,500 waters). All mutations were made from this common point as described above. An approximate surface area was calculated for the protein (based upon a cylindrical representation of the helices), which suggested an approximate number of lipids that should be removed from the monolayer that contained the protein. Lipids in closest contact with the protein were thus removed, leaving a total of 479 lipids along with neutralizing ions (~81,000 total atoms). In order to minimize finite size effects and avoid artifacts of the simulated boundary condition, we chose to use a large, fully hydrated bilayer and to simulate with a variable lateral area. We used the united atom GROMOS force field (GROMACS version 3.3.2), which allows for more efficient simulation of large lipid systems and is more frequently used for variable lateral area simulations than CHARMM. Simulations were performed under the NPT ensemble at 303 K and employed the Parrinello-Rahman pressure and Nose-Hoover temperature coupling scheme. A cut-off of 16 Å was used for van der Waals interactions, and particle mesh Ewald summation was used for long range electrostatic interactions. The time step was 2 fs, and all bonds were constrained using the LINCS algorithm. Membrane simulations were run for 50 ns after a similar minimization and constrained dynamics scheme as employed for the micelle. Although comparison between different force fields can be complicated, a recent exhaustive simulation study suggests that both force fields are reasonably similar in modeling protein behavior (42). In order to confirm that our comparison of micelle and bilayer results was not overly dependent upon our force field choice, we simulated WT αS bound to DOPS using CHARMM (using parameters from Ref. 43) under a constant area

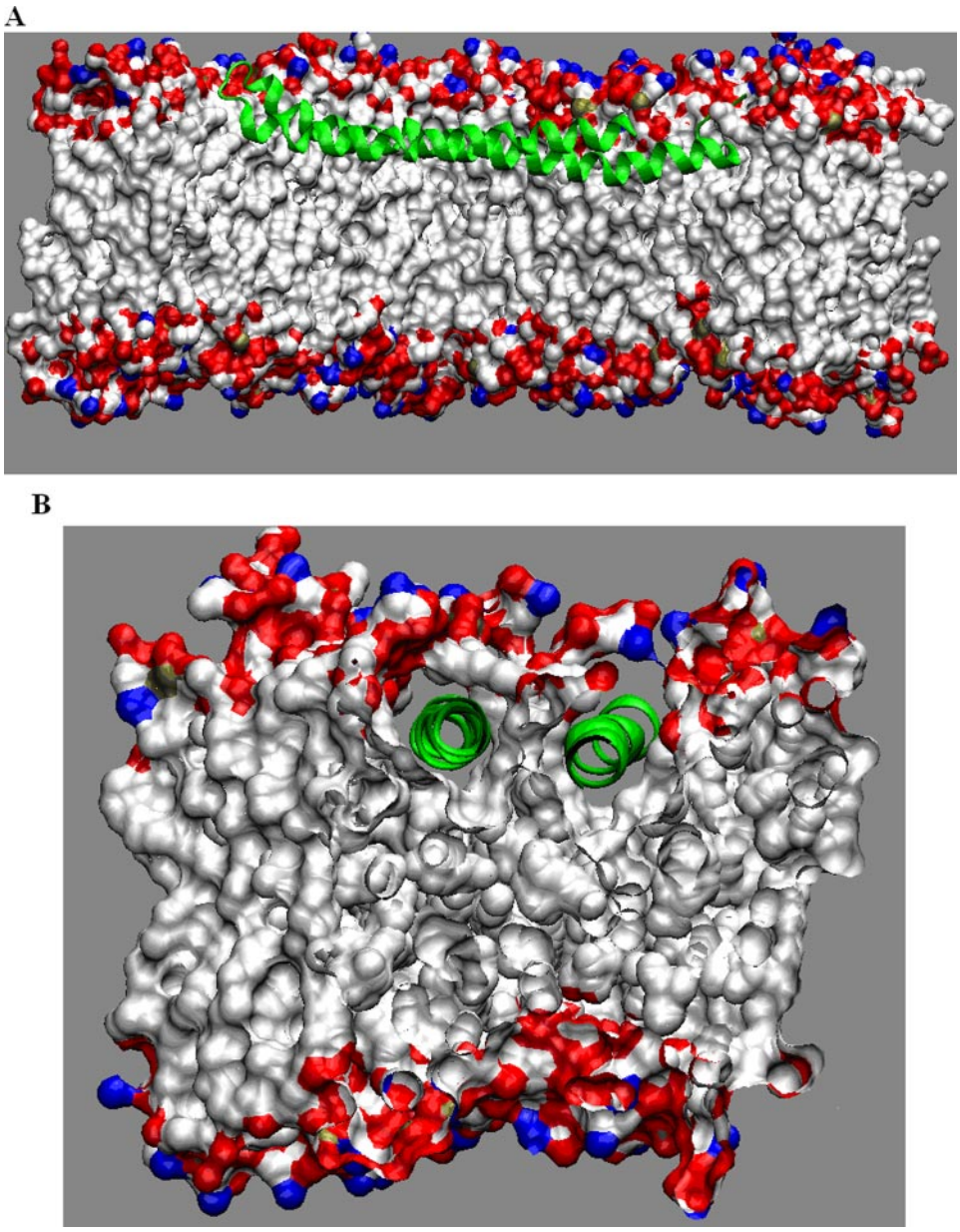

FIGURE 3. **The interaction of αS with a DOPS bilayer.** *A* and *B*, snapshots of wild-type αS bound to the DOPS bilayer, after 45 ns of simulated dynamics. The protein embeds into the hydrophobic core of the bilayer, beneath the lipid headgroup. αS backbone is represented as a *green ribbon*, and the DOPS bilayer is shown with the following *color scheme*: carbon (*white*), oxygen (*red*), nitrogen (*blue*), and phosphorus (*tan*). Hydrogen, water, ions, and lipids have been removed for clarity of presentation.

(NP_NAT ensemble) and observed magnitudes of protein motion remarkably consistent with those we report below for GROMOS (Fig. S1).

Simulations were run on the Minnesota Supercomputer Institute's cluster of 307 IBM BladeCenter LS21 nodes and the University of Illinois' National Center for Supercomputing Application's cluster of 1450 Dell PowerEdge 1750 nodes. Approximately 200,000 total cpu hours were used.

RESULTS

Bound State Structure—Snapshots taken from the simulation of WT αS bound to an SDS micelle are shown in Fig. 2. The backbones of the two helices, consisting of residues 3–37 (helix-N) and 45–92 (helix-C), are both deeply buried beneath the headgroups of the detergent. Despite a high degree of fluctuation, the helices remain stably immersed in these channels throughout the course of all of the simulations. The terminal regions of helix-C are frayed but stable, and the helices themselves follow a somewhat tortuous path through the channels; rarely are they straight. The major features of the NMR structure are conserved throughout the simulations (34). In particular, as illustrated in Fig. 2*C*, the nonpolar side chains orient toward the micelle center, basic side chains (αS is lysine-rich) orient along the micelle surface and form salt bridges with the sulfate headgroups, and the acidic side chains orient into the solvent. A similar motif has been observed in apolipoproteins (44). Within the N-terminal region of αS, there are seven imperfect copies of an 11-mer repeat, most of which contain two (i, $i + 2$) lysine residues. In all cases, these paired side chains point in opposite directions along the micelle surface, exerting a strong influence on helical depth and topology. In agreement with previous observation, the highly hydrophobic sixth 11-mer repeat buries deepest into the micelle (34, 36, 45). This section of the protein is within the largely hydrophobic NAC (residues 60–95), the region that is thought to drive fibril formation (46, 47). Fig. S2 plots the C^α r.m.s.d. from the NMR structure, a quantitative measure of stability and equilibration. Helix-C shows slightly elevated deviation as compared with helix-N, although the values of ~2–4 Å for both are typical for protein simulations and indicate that the structure is equilibrated and the simulations are converged. An indication of the micelle's role in stabilizing α-synuclein's structure, the r.m.s.d. calculated from the simulation of the protein in water (*i.e.* no micelle) reached 12 Å after only 5 ns.

In both the WT and mutant simulations, αS binding significantly perturbs the equilibrium structure of the SDS micelle. As is readily apparent from Fig. 2, *A* and *B*, the micelle flattens into an elongated, ellipsoidal (rodlike) shape. The deformation is quantified by a 20% increase in the radius of gyration (23.6 Å *versus* 19.5 Å in the case of the protein-free micelle). Quantifying the area per headgroup for an irregularly shaped structure,

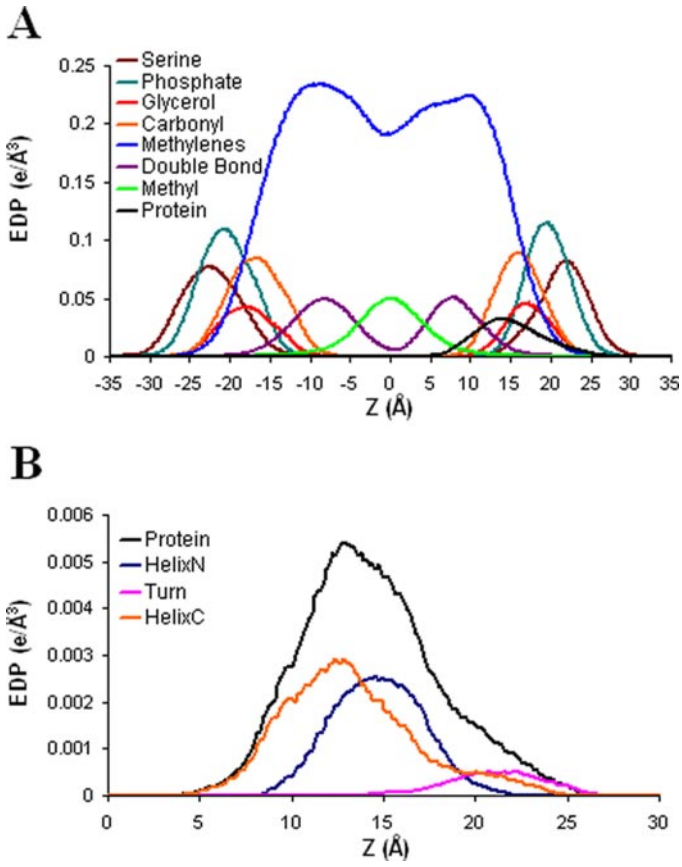

FIGURE 4. **Depth of αS in the DOPS bilayer.** *A*, component electron density profiles (*EDP*) for DOPS bilayer and wild-type αS. *B*, C^{α} electron density, describing relative backbone depth of the protein helices.

such as the micelle, can be done by measuring the solvent-accessible surface area. The change in micelle shape upon αS binding is accompanied by an ~10% decrease in solvent-accessible surface area, a substantial change that will be discussed in detail below. Differences in solvent-accessible surface area between the αS variants were negligible.

Fig. 3, *A* and *B*, shows snapshots of WT αS bound to a negatively charged DOPS bilayer. Over the course of the 50-ns simulation, the helices submerged more than 5 Å more deeply into the bilayer core than their starting positions and flattened significantly. The r.m.s.d. (Fig. S2) suggests that the bilayer simulations are reasonably well converged, although there remain subtle changes in the helix positions throughout the 50 ns.

Fig. 4 presents the electron density profiles for the molecular constituents of the WT system. Electron density profiles are commonly used to describe the location of molecules and their chemical components within a bilayer. The figures indicate that the two helix backbones are submerged just beneath the lipid headgroup/water interfacial region, allowing the hydrophobic face of the protein to interact with the lipid hydrophobic core and the hydrophilic face of the protein to interact with the lipid polar region and water. Helix-N ends up at a depth of ~3 Å beneath the lipid headgroup phosphates, in agreement with a recent experimental study (48). Helix-C buries an average of ~2 Å deeper into the bilayer center than helix-N despite having started at the same depth. This result is consistent with our micelle simulation and previous studies (34, 36, 45). As in the micelle-bound state, the turn region projects outward from the bilayer. This molecular architecture leads to a substantially different binding environment for the protein in the bilayer (Fig. 3*B*), as compared with the micelle (Fig. 2*C*). In contrast to the micelle, portions of the protein are fully ensconced in the lipid (a subset of the lipid headgroups hang over the helices and directly interact with the polar side chains). Thus, the protein appears in places to tunnel through the bilayer, although there are regions where the protein is also exposed to the water. This additional degree of incorporation may underscore a tighter interaction with the lipids than detergents and probably explains an overall decrease in dynamics of the bilayer-bound proteins, as described below.

Protein Dynamics—The simulations provide insight into similarities and differences in how the micelle and bilayer affect dynamic deviations from the average NMR structure for the WT and mutant proteins. The root mean square fluctuation (r.m.s.f.) provides a quantitative measure of a protein's C^{α} motion on a per residue basis and a first look at changes induced by the mutations. Fig. 5*A* compares the r.m.s.f. for the micelle-bound WT with the A53T, A30P, and E46K mutants. Consistent with experimental measurements, the maximal dynamics of the WT protein occur in the nonhelical regions: the N and C termini of the protein as well as the turn (residues 38–44) for each of the proteins for which experimental data is available (10, 34). The first two residues of the N terminus interact intimately with the detergent, whereas the C-terminal residues downstream of Gly^{93} extend out of the micelle, into the water, causing a sharp increase in r.m.s.f. (data have not been included in the graph). The r.m.s.f. also indicates a high degree of flexibility near residues Gly^{67} and Gly^{68} as well as downstream of Gly^{82} and Gly^{84}. Interestingly, the WT r.m.s.f. is greater in the helix-kinking region of Gly^{67}/Gly^{68} than in any of the mutants, with the greatest reduction in the case of A30P. As would be expected, there is a clear maximum and subtle increase over WT in the dynamics around the site of the proline substitution. Less expected is an increase in dynamics in that same region in the E46K mutant, with a maximal value at residue 24. E46K dynamics are reduced immediately upstream of position 46, in the turn region. A30P and E46K display less dynamics throughout helix-C, suggesting that this measure cannot be directly correlated with experimental binding affinity. The threonine substitution behaves similarly to the WT, although there is a subtle decrease in dynamics in helix-N and in helix-C near Gly^{67}/Gly^{68} as well as a slight increase in dynamics at Gly^{82}/Gly^{84}. Direct comparison of simulated αS dynamics to experiment is made through the NMR-measured S^2 (10, 34). Fig. S3 shows S^2 data from the simulations, overlaid with the experimental data for WT, A53T, and A30P (10, 34). Experimental results for E46K have not yet been published. Although direct comparison between the experiments and simulation is difficult, and although there are some elements of the simulation that do not exactly reproduce the experimentally observed behavior, all of the major trends upon which our results are based are reasonably consistent with experiments (49).

Fig. 5*B* shows r.m.s.f. data for the bilayer-bound αS variants and indicates an overall decrease in protein dynamics of 2–3-fold as compared with the micelle-bound forms. We have

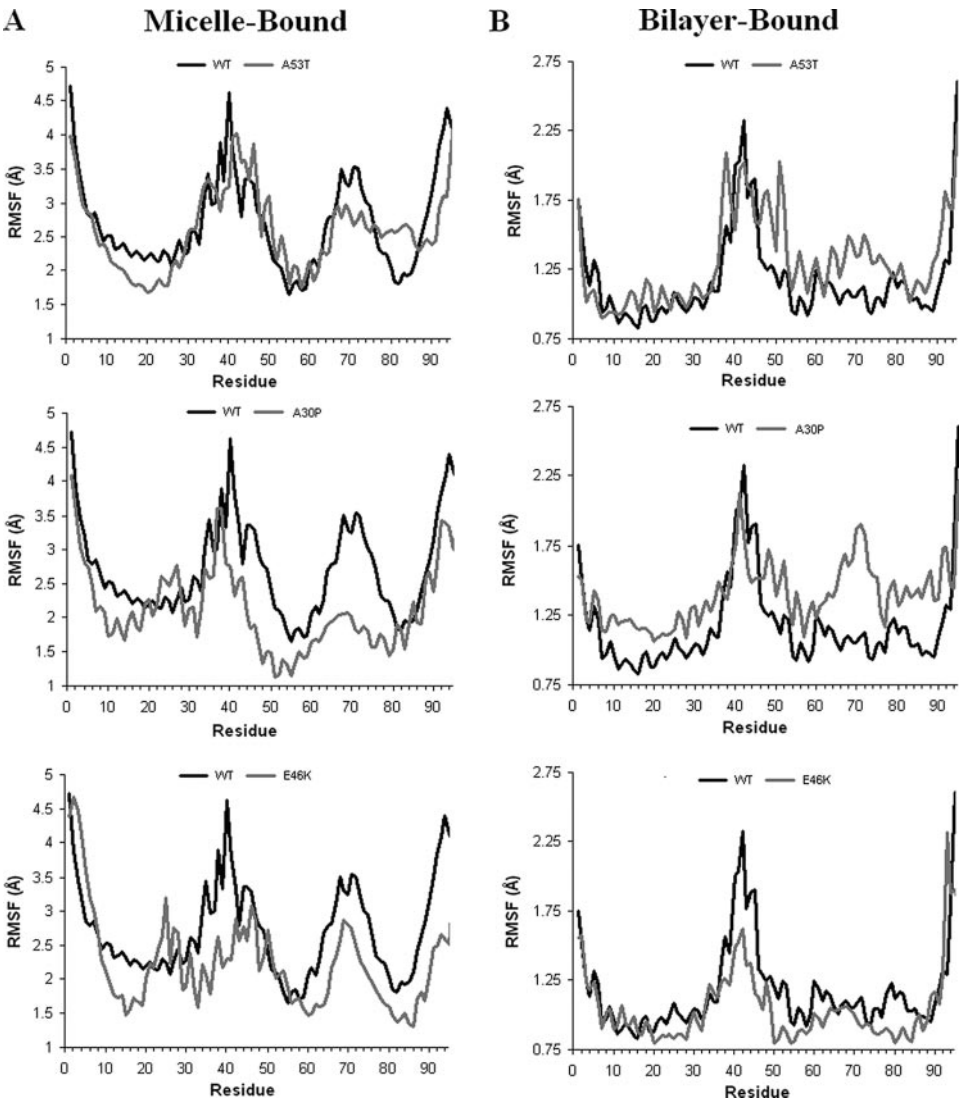

FIGURE 5. **Structural dynamics of the micelle- and bilayer-bound forms.** Shown is the r.m.s.f. of αS C^{α} calculated from the eight simulations, in each case averaged over the last 25 ns for the micelle-bound (*A*) and bilayer-bound (*B*) states.

checked to ensure that this reduction is not due to the different force fields (as stated under "Materials and Methods"). A comparison between GROMACS and CHARMM bilayer-bound dynamics is given in Fig. S1; the similarity in magnitudes justifies comparison of our micelle- and bilayer-bound simulations. The general features of the bilayer-bound r.m.s.f. data are broadly similar to the micelle forms; the largest maximal values are in the nonhelical segments and the turn. Remarkably, a maximum is seen at the Gly^{67}/Gly^{68} hinge in all variants except the WT, where it has completely vanished (the r.m.s.f. curve is concave for the mutants but flat for the WT). The micelle trends for A53T and A30P are reversed in the bilayer; both display an *increase* in their overall dynamics (relative to WT). In contrast, the E46K mutant displays a slight suppression of dynamics. As is always the case with simulation, these trends might change given significantly longer time scales.

A subset of the overall dynamics, helical bending is of particular interest. Bending can reflect at least two things: 1) equilibrium fluctuations that tightly couple the shape of the helices to that of the highly malleable micelle or more rigid bilayer or 2) perturbation induced by mutation that disrupts these normal interactions. Helical bending was calculated at each residue as the angle between the two helical axes formed by the residues four upstream and four down-stream, and the results for the micelle-bound states are given in Fig. 6*A*. Both the WT and A53T protein show minimal bending in helix-N, whereas the A30P and E46K mutants bend significantly (as much as 40° in A30P and 25° in E46K). In the A30P protein, this increase occurs upstream of the substitution (maximally at position 25), where it is, on average, approximately twice as bent (~40°) as the WT is at its position of maximum bending (just downstream of Gly^{67}/Gly^{68}). In helix-C, the proline substitution has a significant effect in reducing the bend around Gly^{67}/Gly^{68}, indicating long range effects that act through the detergent. In contrast, the E46K system displays a large increase in bending in helix-C. In the A53T mutant, the bending is of roughly the same magnitude as the WT. The A53T mutant also shows increased bending at Gly^{82}/Gly^{84} in helix-C. Collectively, the effects of each mutation on the r.m.s.f. and bending in the micelle-bound form indicate that the two helices are not fully independent, despite being physically sequestered by the detergent.

Helical bending in the bilayer-bound state is shown in Fig. 6*B*. In helix-N, A30P displays an increase in bending, at approximately the same location as in the micelle-bound state, although slightly lower in magnitude. Similarly, the WT and A53T mutants show minimal bending in helix-C. However, in contrast to the micelle-bound state, E46K shows minimal bending in helix-N. The bending in helix-C is entirely different in the bilayer-bound state than in the micelle-bound form. Whereas in the micelle-bound structure each protein showed an increase around Gly^{67}/Gly^{68}, in the bilayer-bound form, only A30P shows a small increase in bending at that point. A30P also shows a small increase in bending around Gly^{82}/Gly^{84}. Interestingly, the WT shows a maximal bending value at residue 60, a position in which bending is not observed in the micelle-bound state.

Fig. 7 shows a time series of the changes in bending angle at the position of Gly^{67}/Gly^{68} from the WT micelle-bound and bilayer-bound simulations. Snapshots illustrate the extreme values, as

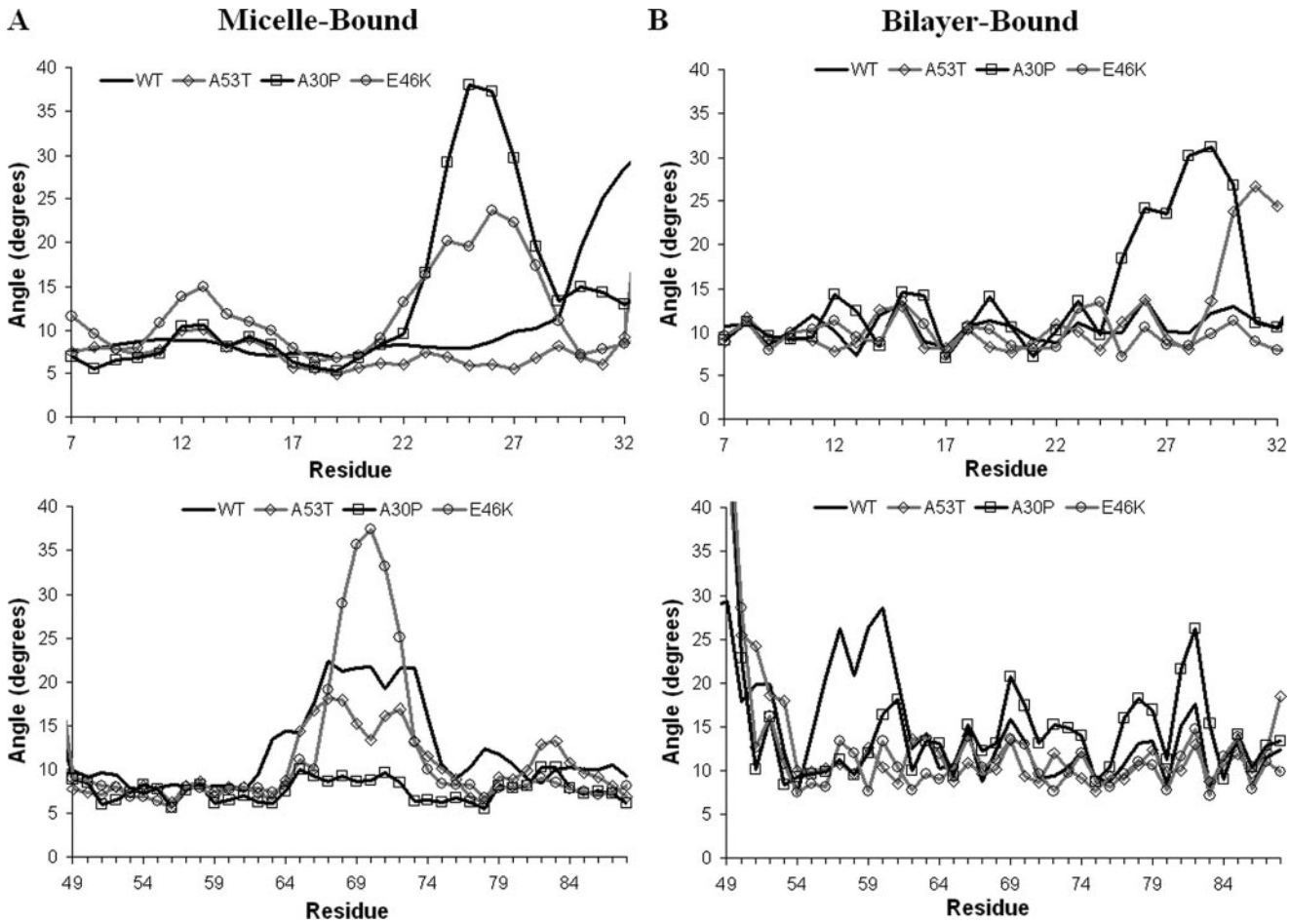

FIGURE 6. **Helical bending.** The angle formed by the intersection of the residues four up- and downstream at each helical position describes the structural adaptation of the protein to the environment for the micelle-bound (*A*) and bilayer-bound (*B*) states.

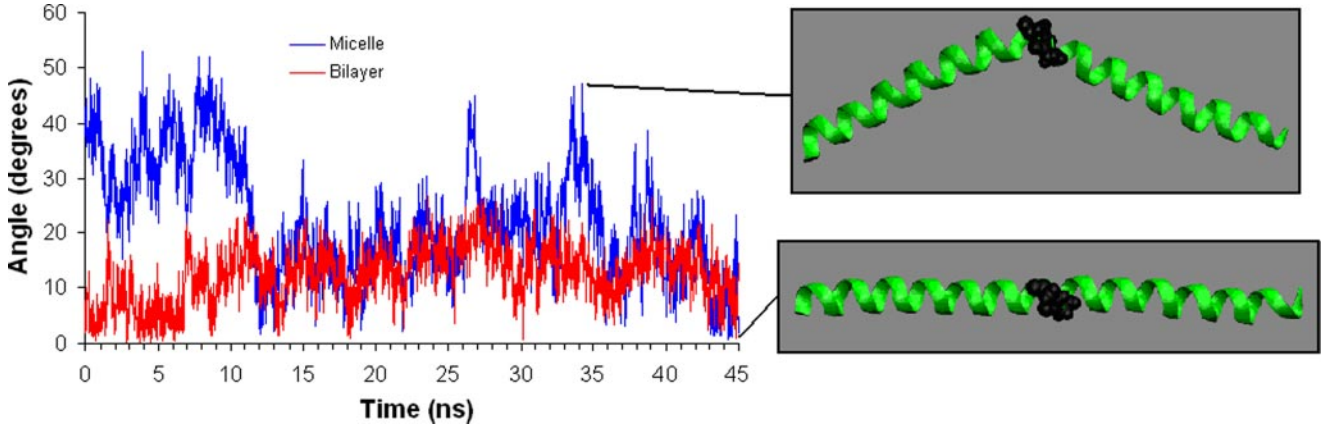

FIGURE 7. **Helical bending at Gly^{67}/Gly^{68} is highly dynamic.** The bending angle at Gly^{67}/Gly^{68} was calculated at each time point in helix-C, as described under "Results," for the micelle-bound (*blue*) and bilayer-bound (*red*) states. The micelle-bound state shows a large range of values, capturing nearly straight as well as highly bent structures, whereas the bilayer-bound state remains relatively straight. Representative snapshots from the micelle-bound state at the indicated time points show minimal and maximal bending conformations (the micelle, water, and ions have been omitted). The helix is represented as a *green ribbon*, and Gly^{67}/Gly^{68} are shown in the *space-filling representation* as *black*.

the micelle-bound helix fluctuates between nearly straight and highly bent. The bilayer-bound protein equilibrates at a relatively low angle (~15°). It is highly interesting that in the latter part of the simulations, the average bending is similar in the two environments, perhaps suggesting that the protein itself has this as its preferred state. Consistent with the overall increase in r.m.s.f., however, the micelle-bound form samples a wider range of angles. These lower angles are about half that of the averaged NMR structure, probably a consequence of the simulated micelle being larger than the experimental average.

A30P: Destabilization and Unfolding—The proline substitution is known to alter the helical content of αS (9, 10, 13, 16), and the simulations reproduce this result. Fig. S4 plots helical content on a per residue basis for the micelle-bound A30P pro-

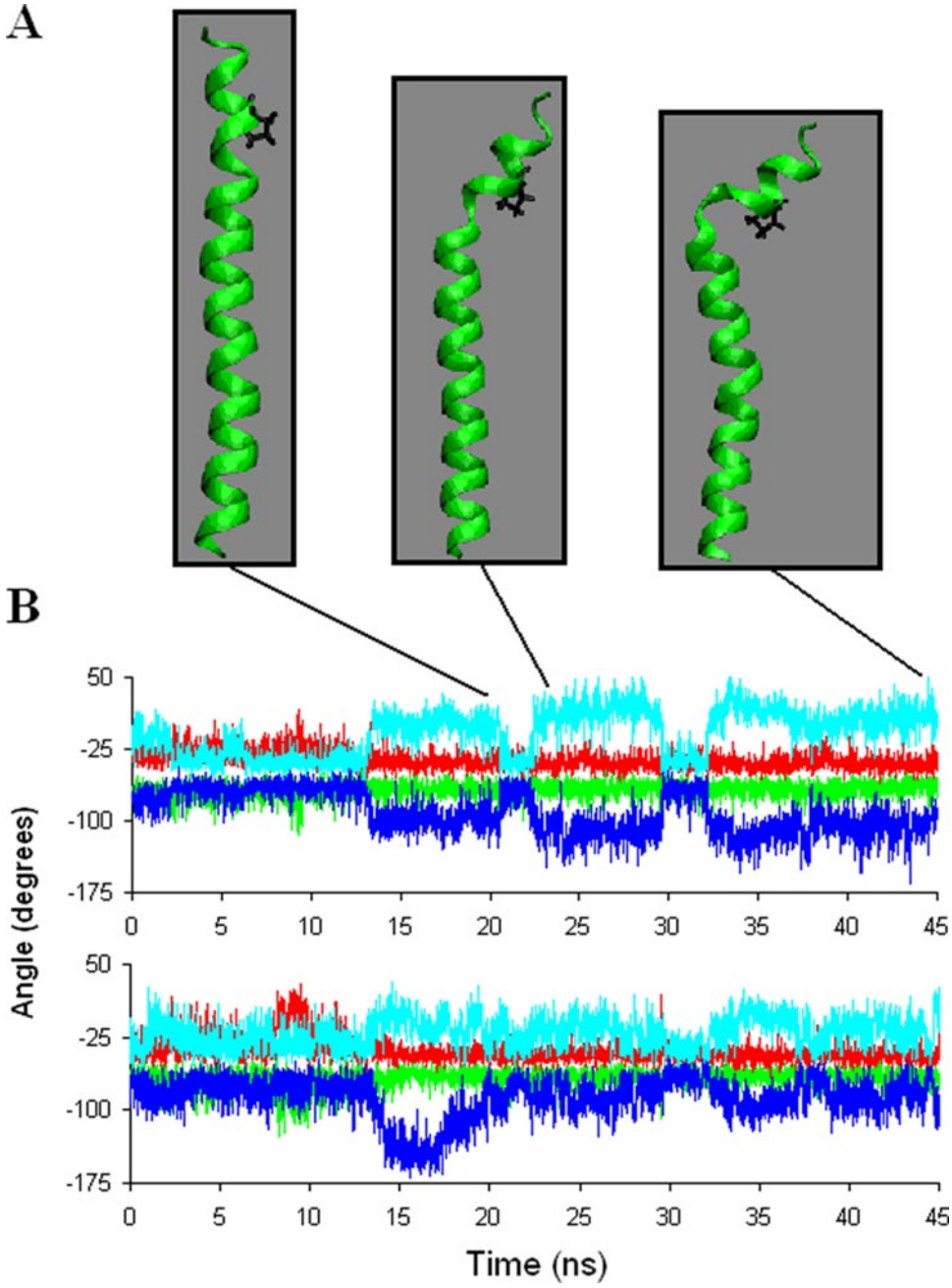

FIGURE 8. **The A30P mutation causes a decrease in helicity.** *A*, snapshots illustrating different conformations of the A30P mutant from the micelle-bound simulation: straight helix, kinked helix, and unfolded (time points 21, 24, and 45 ns). Helix-N is represented as a *green ribbon*, and the proline is shown in *black* (micelle, water, and ions omitted). *B*, torsion angles for the A30P substitution mutant and wild-type protein for residues 26 and 28 from the micelle-bound simulations show reversible unfolding. The color scheme is as follows: WT phi (*green*), WT psi (*red*), A30P phi (*dark blue*), A30P psi (*light blue*).

tein compared with the WT. In all simulations, the turn region is completely without secondary structure. Consistent with the r.m.s.f. and bending data, helicity is disrupted upstream of the proline substitution. Snapshots in Fig. 8*A* illustrate three loosely defined categories of helical structure observed in micelle-bound A30P: straight, kinked, and unfolded (*i.e.* loss of i, $i + 4$ hydrogen bonding and change in geometry including backbone torsion angles). There is no significant reduction in helicity in the micelle-bound forms of A53T or E46K mutants, also consistent with experiments (9, 10, 13, 16, 18, 21).

Another way to present these dynamic transitions is through the time evolution of backbone torsion angles. During a 15-ns pre-equilibrated period of dynamics, there were significant deviations in the WT from typical α-helical torsion angles in certain residues (Fig. S5). Throughout the remainder of the simulation, the WT protein displayed torsion angles for all residues that are close to that of a typical α-helix ($\varphi \approx -62°$, $\psi \approx -41°$ (19)). The proline substitution induces substantial deviations from helicity, in particular at Val^{26} and Glu^{28}. Fig. 8*B* overlays the results for residues 26 and 28 in the micelle-bound WT and A30P. Ala^{27} and Pro^{30} show more subtle variation (Fig. S5), as do residues Gly^{25}, Thr^{33}, and Lys^{34} (data not shown). The time evolution of these structural fluctuations is illuminating, showing a dynamic volley between unfolded and helical; unfolded regions can refold on the nanosecond time scale, particularly evident at residue 26. The structural transitions back to a helical state for this residue, however, appear to mostly dissipate toward the end of the simulation, suggesting that the secondary structure may be fully broken by this point. It is not clear, given the brevity of our simulated time scale, whether these transitions will continue or whether the equilibrium structure is indeed completely unfolded at this or other sites. Given the experimental evidence for the latter and the data in Fig. 8, it is likely that unfolding of the bound A30P nucleates at residue 26 but does not extend beyond 4–5 residues up- or downstream of the mutation site. Whether this unfolding would lead to unbinding, given a significantly longer simulation, remains an open question. A comparison of the time-dependent changes in torsion angles and helical bending directly correlates A30P unfolding with maximum bending angles in the N-terminal helix (data not shown). This is in contrast to the high bending angles at Gly^{67}/Gly^{68}, which are not accompanied by a loss of helicity.

The A30P bilayer-bound simulation shows only minor unfolding. Figs. 5 and 6 showed an increase in the backbone r.m.s.f. and helical bending relative to the WT, suggesting that the mutation destabilizes the protein in the same region as in

the micelle-bound simulation. However, the helicity and backbone torsion angles are only subtly affected (data not shown). In this case, it must be noted that equilibration in bilayers is probably a slower process, given the relative relaxation rates of the lipids and detergent, and, as a result, the time scale for full unfolding in the bilayer is possibly longer than we are able to simulate. Torsion angle dynamics for A53T are indistinguishable from WT in both environments; there are no unfolding transitions. This lack of gross structural change agrees well with experimental observation (9, 10, 13, 16, 18). Structural analysis of side chain orientation also reveals no discernable differences between the A53T mutant and the WT (data not shown). Helicity is preserved in E46K and all of the bilayer simulations, with only subtle deviations in torsion angles (data not shown).

A53T: Intra- and Intermolecular Hydrogen Bonding—Recent NMR results measuring protein dynamics at longer time scales (nano- to milliseconds) have suggested that the micelle-bound A53T mutant includes an unresolved, enthalpically stabilizing motif (10). Indeed, Fig. 9 reveals that the secondary structure of helix-C is probably stabilized in the A53T mutant by an intraprotein hydrogen bond that forms between the threonine hydroxyl and the backbone carbonyl of Val^{49}. Fig. 9*A* plots a time series that illustrates the dynamics of this partnership in the micelle-bound system. The hydrogen bond was not present at the onset of the simulation. In fact, during the pre-equilibration period (<15 ns), the hydroxyl group was stabilized by interactions with the SDS and surrounding water. This clearly indicates that the hydrogen bond is not a product of the initial starting configuration but rather the natural, equilibrated structural motif for A53T. Fig. 9*B* shows that the same side chain-backbone hydrogen bond forms in the bilayer-bound simulation of A53T; however, it is noticeably less stable, flickering on and off throughout the simulation. Instead, a different stabilizing interaction predominates; the hydrogen bond forms with the lipid's glycerol backbone carbonyl. SDS has no hydrogen bond acceptors beneath the micelle surface that can compete for threonine's donor hydrogen in this way.

E46K: Putative Increase in Binding Affinity—The E46K substitution leads to an additional intermolecular interaction that is very similar in both environments. As illustrated in Fig. 10, the substituted lysine side chain interacts with the SDS headgroup or the lipid hydrogen bond acceptors (primarily the carbonyl groups) as well as with water throughout the course of the simulation. No intraprotein interaction is observed. Although this interaction probably contributes to the E46K mutant's increased membrane affinity, it has also been suggested that a structural rearrangement may contribute (20). In the micelle-bound simulation, there is an increased interaction between the micelle and the protein turn region (residues 38–44), which is reflected in the decrease in r.m.s.f. (Fig. 5*A*). Long range changes in the r.m.s.f. (*i.e.* far from the mutation) suggest a global change in dynamics, in agreement with a recent experimental study (21). Significantly, in the bilayer-bound state of E46K, helix-C buries ~1–2 Å deeper than WT, although helix-N appears to submerge to the same depth as WT.

DISCUSSION

As regards function and pathology, the behavior of αS on the surface of membranes has been the source of considerable uncertainty. Several studies have concluded that αS aggregation is triggered by interaction with membranes (11, 50, 51), whereas others suggest that membrane interaction inhibits the process (52). Thus, as is the case with most membrane proteins, the dynamic behavior in the membrane environment is critical to function but is only partially understood (53). Recent NMR data, however, have revealed highly informative and intriguing dynamic information in the case of WT αS, A30P, A53T, and E46K. Indeed, it appears that the dynamics of αS, which were described as "unusually rich" (34), may be the critical piece in understanding the breadth of its interactions and behaviors.

Our efforts to understand the structure and dynamics of the A30P, A53T, and E46K mutants start with a detailed characterization of the WT. αS is a widely studied, presynaptic protein with an unknown physiological function. Recently, it has been suggested that αS inhibits synaptic vesicle fusion after the docking of synaptic vesicles to the presynaptic terminal membrane (28). Relative to other subcellular, membranous structures (such as lysosomes and endosomes), presynaptic vesicles are quite small and are thus characterized by a higher degree of curvature. αS binds to lipid membranes, with highest affinity in the case of small, highly curved vesicles, and this interaction is thought to be tightly coupled to the protein's structure (31, 54, 55). Indeed, the NMR structure supports this notion, demonstrating that the protein itself has a propensity to shadow the binding surface of a micelle by adopting a highly curved, helical structure (34).

In general, the spontaneous curvature of a membrane's component lipids is a significant factor in determining its fusogenic properties (56). The curvature of a bilayer can be altered by the binding of a protein, which can either induce or relieve curvature stress (57). Curvature stress is caused by a discrepancy between the intrinsic, spontaneous curvature of a subset of the component lipids and the actual shape of the bilayer. For example, a subset of the lipids may prefer to sit in a flat bilayer (*e.g.* those with a headgroup cross-sectional area similar to that of their chains) but be forced into a curved structure by the other lipids (*e.g.* those with a headgroup area less than their chains). Those flat-loving lipids would then be in a frustrated, or stressed, state. Area per headgroup, which is directly related to the intrinsic curvature, thus becomes a critical parameter in understanding the fusogenic tendencies of biological membranes.

Curvature stress is exploited by cells, allowing their membranes to overcome a thermodynamic barrier (high energy intermediates) to fusion (56). Membranes with high curvature stress are more likely to fuse with a flatter, target membrane in order to relieve that stress (the larger headgroup lipids will have found a more comfortable home). Likewise, any perturbation that ameliorates curvature stress lowers a membrane's propensity to fuse. One example of how a protein can alter curvature stress is the case of synaptotagmin-1, which encourages fusion of synaptic vesicles by inducing positive curvature in the rela-

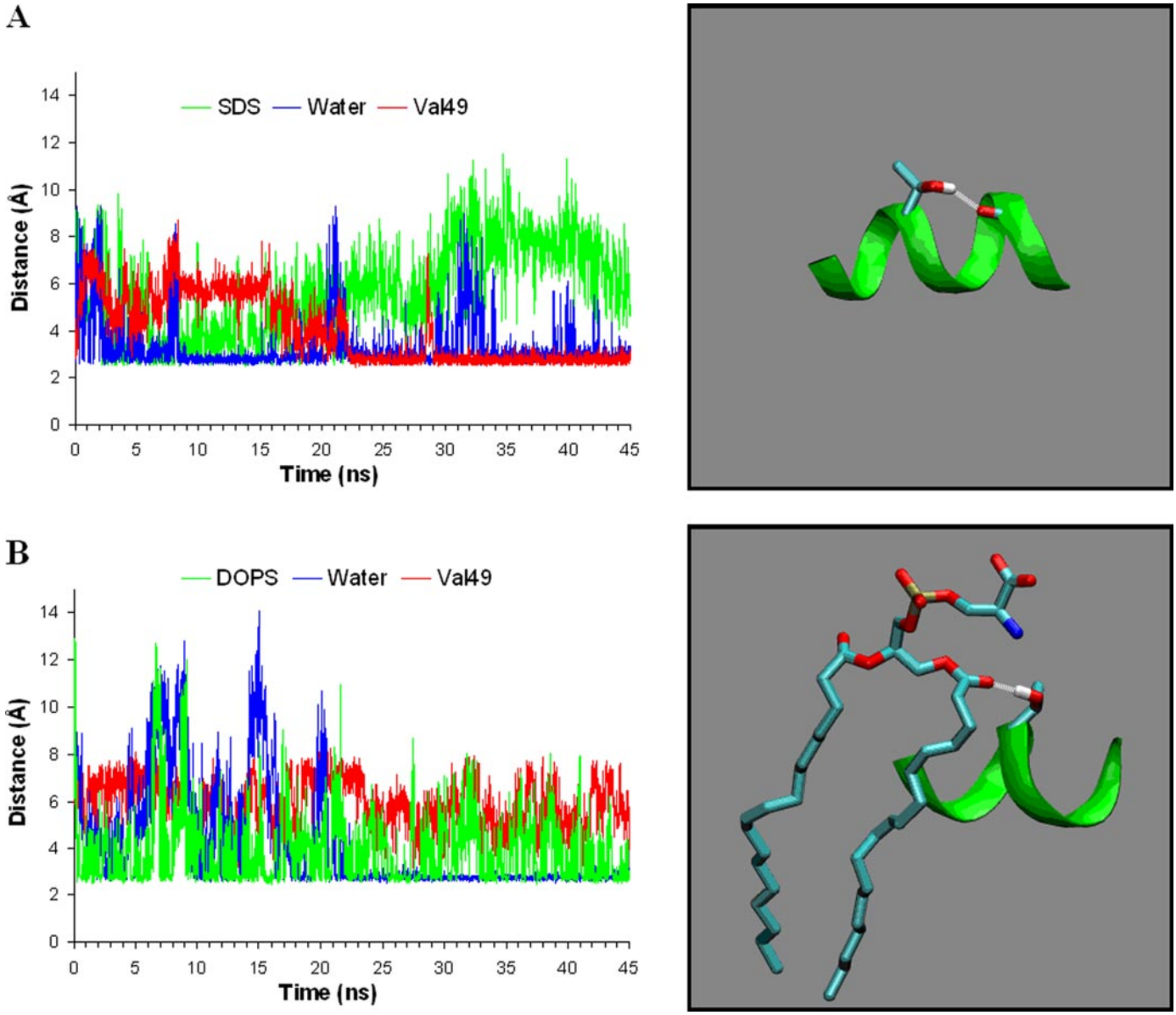

FIGURE 9. **Hydrogen bonding in the A53T mutant stabilizes the helicity.** *A*, minimum distance between Thr^{53} side chain donor oxygen and water oxygens (*blue*), SDS oxygen hydrogen bond acceptors (*green*), and Val^{49} backbone carbonyl oxygen (*red*). Shown is a representative snapshot illustrating the hydrogen bond between the Thr^{53} side chain and Val^{49} backbone taken from the micelle-bound simulation. *B*, minimum distance between Thr^{53} side chain donor oxygen and water oxygens (*blue*), DOPS oxygen hydrogen bond acceptors (*green*), and Val^{49} backbone carbonyl oxygen (*red*). Shown is a representative snapshot illustrating the hydrogen bond between the Thr^{53} side chain and DOPS carbonyl from bilayer simulation. Micelle, bilayer, water, ions, and hydrogens have been omitted for clarity. Backbone is represented as a *green ribbon*; Thr^{53}, Val^{49}, and DOPS are represented with the following *color scheme*: threonine donor hydrogen (*white*), carbon (*light blue*), oxygen (*red*), nitrogen (*blue*), phosphorus (*tan*).

tively flat presynaptic terminal membrane (58). Conversely, as would be relevant to the case of αS binding, synaptic vesicles are typically highly curved (they contain a large fraction of negatively charged lipids as well as lipids with both positive and negative curvature (59)), and existing under curvature stress makes them fusogenic. A decrease in curvature should therefore stabilize the vesicles and inhibit fusion. Consistent with these ideas, a recently introduced theory is that αS binding relieves the curvature stress in small vesicles by reducing packing defects that are thought to occur in highly curved bilayers (54, 55).

MD simulation is a technique well suited for studying the structural and dynamic behavior of membranes and membrane proteins (60–64). Here, we confirm speculation that αS binding significantly deforms a micelle and suggest that a similar mechanism may apply to lipid vesicles (10, 34). It is known that cations can deform spherical (highly curved) SDS micelles into rodlike (flatter) structures (65). By screening the charge-charge interactions between sulfate headgroups, which would otherwise be repulsive, the cations allow the detergent heads to pack closer together, inducing a change in shape. It has been suggested that the lysine residues in αS may have a similar effect (34). Indeed, Fig. 2 showed the elongated micelle structure induced by αS binding, which was quantified by an increased radius of gyration and, perhaps most significantly, a decrease in the solvent-

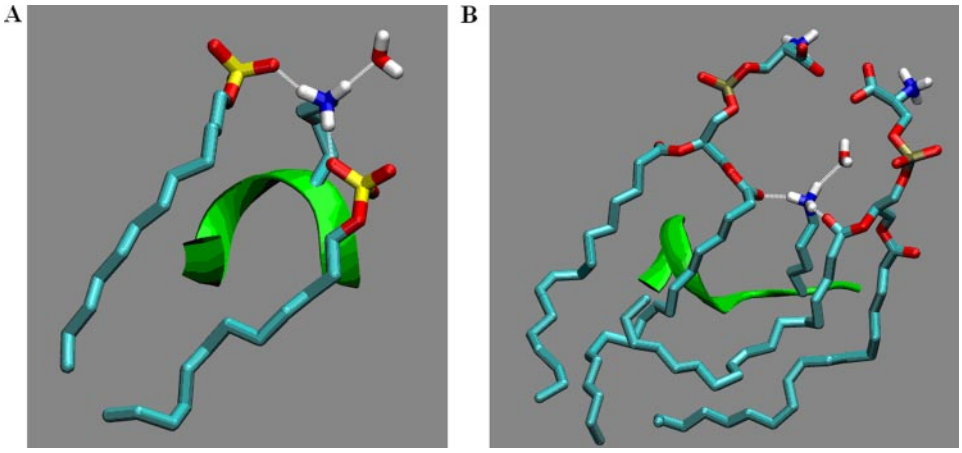

FIGURE 10. **Hydrogen bonding in the E46K mutant.** Representative snapshot illustrating the hydrogen bond between the Lys^{46} side chain and SDS detergent (*A*) or DOPS carbonyl (*B*) and water (other detergent molecules, lipids, water, ions, and aliphatic hydrogens omitted). Backbone is represented as a *green ribbon*; Lys^{46}, SDS, DOPS, and water are represented with the following *color scheme*: hydrogen (*white*), carbon (*light blue*), sulfur (*yellow*), nitrogen (*blue*), and oxygen (*red*).

accessible surface area, which correlates directly with area per headgroup. We note that although the above average size of the micelle results in a slight deviation from sphericity, the difference in structure before and after αS binding is incontrovertible. Our convergent results for WT bending at Gly^{67}/Gly^{68} in the two environments (Fig. 7) suggested that αS itself may have an intrinsic, preferred bend; perhaps it too is in a stressed state when bound intimately to a highly curved micelle or vesicle.

Given our results, we infer a potential mechanism for WT function: αS flattens curved membranes by screening the repulsive interactions between negatively charged, acidic headgroups, thereby reducing the effective area per headgroup and relieving the inherent positive curvature of the lipids on the outer leaflet of the vesicle. This process ameliorates the driving force for fusion. Future simulations of curved bilayers should be aimed at addressing this possibility, although such efforts will probably require significantly more computer power than is currently available. Regarding the mutants, then, we hypothesize that reduced binding of A30P could decrease this inhibitory action of αS, potentially leading to overactive neural signaling. Both the threonine and lysine substitutions are shown to increase direct interaction with the lipids through a hydrogen bond, which may then increase the protein's inhibitory potential.

The deformation of the micelle also serves to maximize both the favorable hydrophobic contact between the rather long helices and the core of the micelle as well as the stabilizing electrostatic interactions between the sulfates and lysines (51). The helices of αS are highly pliable, particularly around Gly^{67}/Gly^{68}, where they exhibit particularly high dynamics and helical bending. This is within the highly hydrophobic NAC (residues 60–95), which we and others observe to bury deeply into the core of the micelle/bilayer (10, 36, 45). Therefore, the simulations suggest that αS bends in order to maximize the contact area between the NAC region and the micelle.

Each mutation and environment has a distinct effect on the average magnitude of helical bending near Gly^{67}/Gly^{68}; relative to the WT, the micelle-bound A30P mutant suppresses bending, the E46K enhances bending, and A53T has little effect. If WT αS bends at Gly^{67}/Gly^{68} in order to maximally insert the hydrophobic NAC region into the micelle center, then modulation of this bending may affect the amount of favorable interaction between protein and micelle. Therefore, changes in bending at the position of Gly^{67}/Gly^{68} may contribute to the observed increased affinity of E46K, the decreased affinity of A30P, and the unchanged A53T affinity (9, 12, 13, 16, 20). Our results suggest that this bending is less prevalent (at least on this time scale) in flat membranes.

In the region of the threonine substitution, the dynamics are nearly identical to those of the WT. This agrees with experiments that concluded that the dynamics on this time scale and the structure of αS are not affected by the A53T mutation (9, 10, 13, 16, 18). However, experiments report a decrease in dynamics near the A53T mutation, on the nano- to millisecond time scale, outside the range of MD simulation (10). How might A53T increase the stability of the helical state? It was pointed out in the NMR study that augmented $^{13}C^{\alpha}$ secondary shifts at the point of the threonine substitution are consistent with an increased helicity and that this goes against the tendency for Ala → Thr mutations to destabilize secondary structure due to decreased entropy of the Thr side chain relative to alanine. Indeed, Ulmer *et al.* (10) speculated that a compensating, enthalpic interaction must be responsible for this helix stabilization. We have found that a hydrogen bond between the threonine and the backbone carbonyl positioned four residues upstream may be responsible for this stabilization. In the micelle-bound state, this intraprotein hydrogen bond is highly stable, whereas in the bilayer-bound state, it competes with hydrogen bond acceptors in the lipid interface region, which may serve to stabilize the bound state of that mutant.

The E46K mutation removes a negative charge that presents a repulsive interaction in the WT. Therefore, this substitution is thought to cause an increase in electrostatic interaction (with SDS or PS) that may explain the observed increase in affinity of the E46K mutant for vesicles containing negatively charged lipids (20). Indeed, the substituted lysine side chain directly interacts with the micelle/bilayer, although in the case of the bilayer, the hydrogen bond is formed most frequently with the carbonyl group and less frequently with the lipid headgroup, suggesting that the headgroup charge may not fully determine the extent of E46K affinity. Interestingly, both the micelle- and lipid-bound simulations suggest larger scale structural rearrangements that may contribute to an increase in affinity. In the micelle-bound state, we observe increases in dynamics in the N-terminal helix at the same positions where others have observed structural

perturbations (21). In the bilayer-bound state, we observed helix-C to submerge deeper into the bilayer center. This suggests that changes in affinity due to this point mutation may be more complex than simply the addition of a single electrostatic interaction.

In the micelle-bound A30P simulation, we observe a decrease in helicity, as has been observed experimentally (9, 10, 13, 16, 18). However, in the bilayer-bound state, decreased stability is reflected in an increase in backbone dynamics but only slight changes in structure. It is possible that the relative stability of A30P in the bilayer environment represents an equilibrated structure different from in the micelle-bound state. However, an equally likely conclusion is that a longer simulation would be necessary to reach the final unfolded state in the bilayer-bound state.

A main feature of WT αS in the micelle-bound state, namely the large increase in fluctuations near Gly^{67}/Gly^{68} relative to neighboring residues, is, remarkably, completely missing in the bilayer-bound form. We interpret this to mean that αS becomes somewhat locked into a stable conformation (*i.e.* the free energy profile is steeply divergent from this conformation). This suggests that on a surface of intermediate curvature (*e.g.* a synaptic vesicle) the protein may respond by modulating the character of fluctuation at this hinge location. Does membrane curvature act as a switch that liberates or dampens relative fluctuations at this glycine hinge? Is this effect all-or-none, or do intermediate degrees of fluctuation exist depending upon the degree of curvature?

Although each simulation began with an identical starting configuration, the equilibrium structures and dynamics of the mutants show deviations from WT that are highly informative. Each mutant does have its own particular local influence (*i.e.* at position 30, 46, or 53), but there is also one common, long range effect. In the bilayer only, the r.m.s.f. curve for each mutant recovers the local maximum at the Gly^{67}/Gly^{68} hinge point that was lost in the WT (Fig. 5). We are left with an unresolved question; does this commonality suggest a functional significance? Although we must entertain the possibility that this result could be due to limited sampling of conformational space, we find it remarkable that these fluctuations are only absent in one of the eight simulations presented in Fig. 5. Importantly, we also note the absence of these fluctuations in the WT, bilayer-bound CHARMM simulation (see Fig. S1), which increases our confidence that this is a real phenomenon.

A highly curved micelle surface and a flat bilayer patch represent two possible extremes of curvature. On the relatively flat bilayer surface, helical bending and dynamics of αS are considerably reduced as compared with the micelle-bound state. We therefore conclude that the extent of αS bending on highly curved surfaces (*e.g.* a micelle) is largely imposed by the curvature of the substrate and that a defining, specifically evolved aspect of the primary sequence of αS is this inherent ability to adapt its structure. We have, in part, addressed the ways in which the familial PD mutants influence this adaptivity, although the exact relationship between αS curvature, dynamics, functionality, and PD pathogenesis remains elusive.

Acknowledgments—The initial coordinates for a smaller SDS micelle were kindly provided by Himanshu Khandelia and Yiannis Kaznesis. We thank Ad Bax, Tobias Ulmer, Lennart Nilsson, Alan Grossfield, and members of the Sachs laboratory for helpful discussion; Sagar Pandit and See-Wing Chiu for GROMOS PS parameters; and Emad Tajkhorshid and Zenmei Ohkubo for CHARMM PS parameters. Computational resources were provided by the Minnesota Supercomputer Institute, the University of Illinois' National Center for Supercomputing Application, and IBM.

REFERENCES

1. Spillantini, M. G., Crowther, R. A., Jakes, R., Hasegawa, M., and Goedert, M. (1998) *Proc. Natl. Acad. Sci. U. S. A.* **95,** 6469–6473
2. Kruger, R., Kuhn, W., Muller, T., Woitalla, D., Graeber, M., Kosel, S., Przuntek, H., Epplen, J. T., Schols, L., and Riess, O. (1998) *Nat. Genet.* **18,** 106–108
3. Polymeropoulos, M. H., Lavedan, C., Leroy, E., Ide, S. E., Dehejia, A., Dutra, A., Pike, B., Root, H., Rubenstein, J., Boyer, R., Stenroos, E. S., Chandrasekharappa, S., Athanassiadou, A., Papapetropoulos, T., Johnson, W. G., Lazzarini, A. M., Duvoisin, R. C., Di Iorio, G., Golbe, L. I., and Nussbaum, R. L. (1997) *Science* **276,** 2045–2047
4. Zarranz, J. J., Alegre, J., Gomez-Esteban, J. C., Lezcano, E., Ros, R., Ampuero, I., Vidal, L., Hoenicka, J., Rodriguez, O., Atares, B., Llorens, V., Gomez Tortosa, E., del Ser, T., Munoz, D. G., and de Yebenes, J. G. (2004) *Ann. Neurol.* **55,** 164–173
5. Conway, K. A., Lee, S. J., Rochet, J. C., Ding, T. T., Williamson, R. E., and Lansbury, P. T., Jr. (2000) *Proc. Natl. Acad. Sci. U. S. A.* **97,** 571–576
6. Wood, S. J., Wypych, J., Steavenson, S., Louis, J. C., Citron, M., and Biere, A. L. (1999) *J. Biol. Chem.* **274,** 19509–19512
7. Narhi, L., Wood, S. J., Steavenson, S., Jiang, Y., Wu, G. M., Anafi, D., Kaufman, S. A., Martin, F., Sitney, K., Denis, P., Louis, J. C., Wypych, J., Biere, A. L., and Citron, M. (1999) *J. Biol. Chem.* **274,** 9843–9846
8. Kubo, S., Nemani, V. M., Chalkley, R. J., Anthony, M. D., Hattori, N., Mizuno, Y., Edwards, R. H., and Fortin, D. L. (2005) *J. Biol. Chem.* **280,** 31664–31672
9. Bussell, R., Jr., and Eliezer, D. (2004) *Biochemistry* **43,** 4810–4818
10. Ulmer, T. S., and Bax, A. (2005) *J. Biol. Chem.* **280,** 43179–43187
11. Cole, N. B., Murphy, D. D., Grider, T., Rueter, S., Brasaemle, D., and Nussbaum, R. L. (2002) *J. Biol. Chem.* **277,** 6344–6352
12. Jensen, P. H., Nielsen, M. S., Jakes, R., Dotti, C. G., and Goedert, M. (1998) *J. Biol. Chem.* **273,** 26292–26294
13. Jo, E., Fuller, N., Rand, R. P., St George-Hyslop, P., and Fraser, P. E. (2002) *J. Mol. Biol.* **315,** 799–807
14. Kahle, P. J., Neumann, M., Ozmen, L., Muller, V., Jacobsen, H., Schindzielorz, A., Okochi, M., Leimer, U., van Der Putten, H., Probst, A., Kremmer, E., Kretzschmar, H. A., and Haass, C. (2000) *J. Neurosci.* **20,** 6365–6373
15. McLean, P. J., Kawamata, H., Ribich, S., and Hyman, B. T. (2000) *J. Biol. Chem.* **275,** 8812–8816
16. Perrin, R. J., Woods, W. S., Clayton, D. F., and George, J. M. (2000) *J. Biol. Chem.* **275,** 34393–34398
17. Outeiro, T. F., and Lindquist, S. (2003) *Science* **302,** 1772–1775
18. Conway, K. A., Harper, J. D., and Lansbury, P. T. (1998) *Nat. Med.* **4,** 1318–1320
19. Barlow, D. J., and Thornton, J. M. (1988) *J. Mol. Biol.* **201,** 601–619
20. Choi, W., Zibaee, S., Jakes, R., Serpell, L. C., Davletov, B., Crowther, R. A., and Goedert, M. (2004) *FEBS Lett.* **576,** 363–368
21. Fredenburg, R. A., Rospigliosi, C., Meray, R. K., Kessler, J. C., Lashuel, H. A., Eliezer, D., and Lansbury, P. T., Jr. (2007) *Biochemistry* **46,** 7107–7118
22. Irizarry, M. C., Kim, T. W., McNamara, M., Tanzi, R. E., George, J. M., Clayton, D. F., and Hyman, B. T. (1996) *J. Neuropathol. Exp. Neurol.* **55,** 889–895
23. Maroteaux, L., Campanelli, J. T., and Scheller, R. H. (1988) *J. Neurosci.* **8,** 2804–2815

24. Abeliovich, A., Schmitz, Y., Farinas, I., Choi-Lundberg, D., Ho, W. H., Castillo, P. E., Shinsky, N., Verdugo, J. M., Armanini, M., Ryan, A., Hynes, M., Phillips, H., Sulzer, D., and Rosenthal, A. (2000) *Neuron* **25,** 239–252
25. Cabin, D. E., Shimazu, K., Murphy, D., Cole, N. B., Gottschalk, W., McIlwain, K. L., Orrison, B., Chen, A., Ellis, C. E., Paylor, R., Lu, B., and Nussbaum, R. L. (2002) *J. Neurosci.* **22,** 8797–8807
26. Murphy, D. D., Rueter, S. M., Trojanowski, J. Q., and Lee, V. M. (2000) *J. Neurosci.* **20,** 3214–3220
27. Yavich, L., Tanila, H., Vepsalainen, S., and Jakala, P. (2004) *J. Neurosci.* **24,** 11165–11170
28. Larsen, K. E., Schmitz, Y., Troyer, M. D., Mosharov, E., Dietrich, P., Quazi, A. Z., Savalle, M., Nemani, V., Chaudhry, F. A., Edwards, R. H., Stefanis, L., and Sulzer, D. (2006) *J. Neurosci.* **26,** 11915–11922
29. Lotharius, J., and Brundin, P. (2002) *Nat. Rev. Neurosci.* **3,** 932–942
30. Chandra, S., Chen, X., Rizo, J., Jahn, R., and Sudhof, T. C. (2003) *J. Biol. Chem.* **278,** 15313–15318
31. Davidson, W. S., Jonas, A., Clayton, D. F., and George, J. M. (1998) *J. Biol. Chem.* **273,** 9443–9449
32. Eliezer, D., Kutluay, E., Bussell, R., Jr., and Browne, G. (2001) *J. Mol. Biol.* **307,** 1061–1073
33. Bussell, R., Jr., and Eliezer, D. (2003) *J. Mol. Biol.* **329,** 763–778
34. Ulmer, T. S., Bax, A., Cole, N. B., and Nussbaum, R. L. (2005) *J. Biol. Chem.* **280,** 9595–9603
35. Dedmon, M. M., Lindorff-Larsen, K., Christodoulou, J., Vendruscolo, M., and Dobson, C. M. (2005) *J. Am. Chem. Soc.* **127,** 476–477
36. Mihajlovic, M., and Lazaridis, T. (2008) *Proteins* **70,** 761–778
37. Tsigelny, I. F., Bar-On, P., Sharikov, Y., Crews, L., Hashimoto, M., Miller, M. A., Keller, S. H., Platoshyn, O., Yuan, J. X., and Masliah, E. (2007) *FEBS J.* **274,** 1862–1877
38. Bortolus, M., Tombolato, F., Tessari, I., Bisaglia, M., Mammi, S., Bubacco, L., Ferrarini, A., and Maniero, A. L. (2008) *J. Am. Chem. Soc.* **130,** 6690–6691
39. Drescher, M., Veldhuis, G., van Rooijen, B. D., Milikisyants, S., Subramaniam, V., and Huber, M. (2008) *J. Am. Chem. Soc.* **130,** 7796–7797
40. Humphrey, W., Dalke, A., and Schulten, K. (1996) *J. Mol. Graph. Model.* **14,** 33–38
41. Frishman, D., and Argos, P. (1995) *Proteins* **23,** 566–579
42. Rueda, M., Ferrer-Costa, C., Meyer, T., Perez, A., Camps, J., Hospital, A., Gelpi, J. L., and Orozco, M. (2007) *Proc. Natl. Acad. Sci. U. S. A.* **104,** 796–801
43. Ohkubo, Y. Z., and Tajkhorshid, E. (2008) *Structure* **16,** 72–81
44. Segrest, J. P., Jackson, R. L., Morrisett, J. D., and Gotto, A. M., Jr. (1974) *FEBS Lett.* **38,** 247–258
45. Bussell, R., Jr., Ramlall, T. F., and Eliezer, D. (2005) *Protein Sci.* **14,** 862–872
46. Giasson, B. I., Murray, I. V., Trojanowski, J. Q., and Lee, V. M. (2001) *J. Biol. Chem.* **276,** 2380–2386
47. Iwai, A., Yoshimoto, M., Masliah, E., and Saitoh, T. (1995) *Biochemistry* **34,** 10139–10145
48. Jao, C. C., Der-Sarkissian, A., Chen, J., and Langen, R. (2004) *Proc. Natl. Acad. Sci. U. S. A.* **101,** 8331–8336
49. Buck, M., Bouguet-Bonnet, S., Pastor, R. W., and MacKerell, A. D., Jr. (2006) *Biophys. J.* **90,** L36–38
50. Lee, H. J., Choi, C., and Lee, S. J. (2002) *J. Biol. Chem.* **277,** 671–678
51. Zhu, M., Li, J., and Fink, A. L. (2003) *J. Biol. Chem.* **278,** 40186–40197
52. Narayanan, V., and Scarlata, S. (2001) *Biochemistry* **40,** 9927–9934
53. Sachs, J. N., and Engelman, D. M. (2006) *Annu. Rev. Biochem.* **75,** 707–712
54. Kamp, F., and Beyer, K. (2006) *J. Biol. Chem.* **281,** 9251–9259
55. Nuscher, B., Kamp, F., Mehnert, T., Odoy, S., Haass, C., Kahle, P. J., and Beyer, K. (2004) *J. Biol. Chem.* **279,** 21966–21975
56. Chernomordik, L., Kozlov, M. M., and Zimmerberg, J. (1995) *J. Membr. Biol.* **146,** 1–14
57. McMahon, H. T., and Gallop, J. L. (2005) *Nature* **438,** 590–596
58. Martens, S., Kozlov, M. M., and McMahon, H. T. (2007) *Science* **316,** 1205–1208
59. Takamori, S., Holt, M., Stenius, K., Lemke, E. A., Gronborg, M., Riedel, D., Urlaub, H., Schenck, S., Brugger, B., Ringler, P., Muller, S. A., Rammner, B., Grater, F., Hub, J. S., De Groot, B. L., Mieskes, G., Moriyama, Y., Klingauf, J., Grubmuller, H., Heuser, J., Wieland, F., and Jahn, R. (2006) *Cell* **127,** 831–846
60. Pitman, M. C., Suits, F., Mackerell, A. D., Jr., and Feller, S. E. (2004) *Biochemistry* **43,** 15318–15328
61. Kucerka, N., Perlmutter, J. D., Pan, J., Tristram-Nagle, S., Katsaras, J., and Sachs, J. N. (2008) *Biophys. J.* **95,** 2792–2805
62. Sachs, J. N., Petrache, H. I., and Woolf, T. B. (2003) *Chem. Phys. Lipids* **126,** 211–223
63. Leontiadou, H., Mark, A. E., and Marrink, S. J. (2004) *Biophys. J.* **86,** 2156–2164
64. Tarek, M. (2005) *Biophys. J.* **88,** 4045–4053
65. Garg, G., Hassan, P. A., Aswal, V. K., and Kulshreshtha, S. K. (2005) *J. Phys. Chem. B* **109,** 1340–1346